Journal of Physics D:
Applied Physics

TOPICAL REVIEW • **OPEN ACCESS**

Altermagnetism in epitaxial $NiCo_2O_4$ thin films via higher-order magnetic anisotropy

To cite this article: Hiroki Koizumi and Yuichi Yamasaki 2025 *J. Phys. D: Appl. Phys.* **58** 253002

OPEN ACCESS
IOP Publishing
Journal of Physics D: Applied Physics
J. Phys. D: Appl. Phys. **58** (2025) 253002 (12pp)
https://doi.org/10.1088/1361-6463/addfe2

Topical Review

Altermagnetism in epitaxial $NiCo_2O_4$ thin films via higher-order magnetic anisotropy

Hiroki Koizumi[1,*] **and Yuichi Yamasaki**[2,3]

[1] Center for Science and Innovation in Spintronics (CSIS), Tohoku University, Sendai 980-8577, Japan
[2] Center for Basic Research of Material (CBRM), National Institute for Materials Science (NIMS), Tsukuba, Ibaraki 305-0047, Japan
[3] International Center for Synchrotron Radiation Innovation Smart, Tohoku University, Sendai 980-8577, Japan

E-mail: hiroki.koizumi.d7@tohoku.ac.jp

Received 21 February 2025, revised 15 May 2025
Accepted for publication 3 June 2025
Published 17 June 2025

Abstract

$NiCo_2O_4$ is a ferrimagnetic oxide with an inverse spinel structure that has garnered significant research interest due to its unique properties, including relatively high electrical conductivity, mixed-valence cations, and a Néel temperature exceeding room temperature. Furthermore, epitaxial $NiCo_2O_4$ thin films provide an exciting platform for tuning material properties and uncovering novel phenomena that are not observed in bulk single crystals. In this review, we highlight recent advancements in epitaxial $NiCo_2O_4$ thin films, focusing on: (i) the tunability of anti-site defects through controlled fabrication conditions, (ii) the emergence of easy-cone magnetic anisotropy (ECMA) induced by these anti-site defects, (iii) the realization of a nontrivial spin structure characterized by magnetic toroidal quadrupole order, driven by the ECMA, (iv) novel magneto-transport phenomena arising from this nontrivial spin structure, and (v) the correlation between this nontrivial spin structure and the concept of altermagnetism.

Keywords: altermagnetism, magnetic anisotropy, thin films, $NiCo_2O_4$

1. Introduction

The spinel structure features a crystalline lattice characterized by the space group $Fd\bar{3}m$ (No. 227) and is commonly represented by the chemical formula AB_2O_4 in oxides [1, 2]. This structure consists of two sublattices: a diamond lattice and a pyrochlore lattice, corresponding to tetrahedral (T_d) and octahedral (O_h) oxygen coordination, respectively, as shown in figure 1(a). The T_d sites are shaded blue, while the O_h sites are shaded green. The spinel structure allows for selective site occupancy of A ions, leading to two primary configurations. When A ions predominantly occupy T_d sites, the structure is referred to as a normal spinel. Conversely, when A ions primarily occupy O_h sites, it is known as an inverse spinel. In most spinel oxides composed of $3d$ elements, the inverse spinel configuration is energetically favored [3]. The energy splitting of d-orbitals is significantly influenced by the crystal field generated by the surrounding ligand oxygen ions. At O_h sites, the d-orbitals split into a lower-energy set of three t_{2g} orbitals and a higher-energy set of two e_g orbitals. In contrast, at T_d sites,

* Author to whom any correspondence should be addressed.

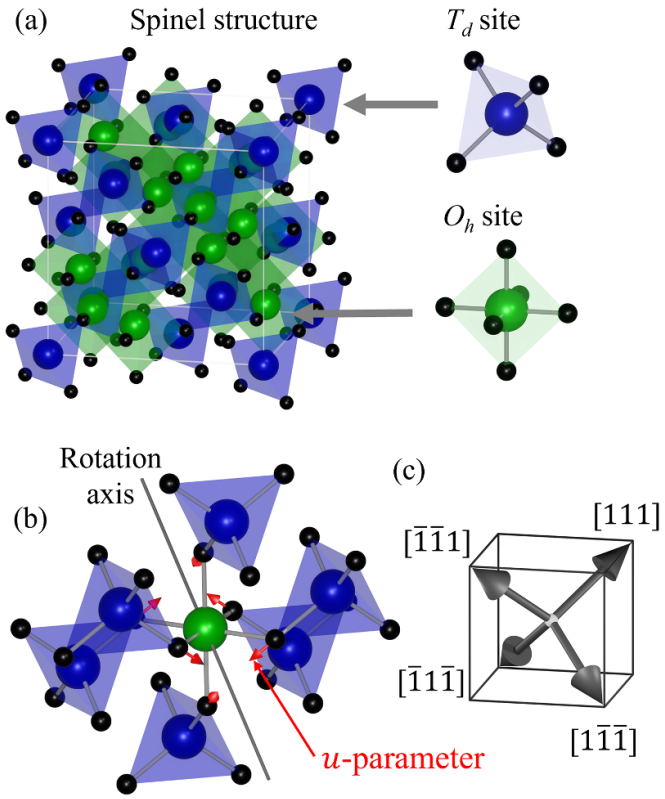

Figure 1. (a) The schematic image of the spinel oxide. Blue, green, and black ions correspond to T_d-site, O_h-site, and oxygen ions, respectively. (b) The relations between the three-fold rotational axis and u-parameter of the surrounded O_h site of $NiCo_2O_4$. (c) Four non-equivalent axes with three-fold rotational axis symmetry in the spinel structure.

they split into a higher-energy set of three t_2 orbitals and a lower-energy set of two e orbitals [4]. This variation in electronic states between T_d and O_h sites plays a critical role in determining the magnetic properties of spinel oxides.

Many spinel oxides are collinear ferrimagnets, where the spin moments of T_d and O_h site ions are aligned in opposite directions. However, some spinel magnets exhibit more complex spin ordering due to competing magnetic interactions arising from geometric frustration [5, 6]. The first theoretical study of noncollinear spin structures was conducted by Yafet and Kittel [7], who demonstrated that a triangular spin configuration could be a ground state under magnetic frustration. Kaplan *et al* further developed this model, showing that a triangular spin configuration becomes stable in tetragonally distorted spinels [8–12]. On the other hand, antiferromagnetic coupling within the pyrochlore sublattice, a geometrically frustrated lattice, induces competing interactions and leads to the emergence of noncollinear spin structures [13–20]. For example, $CoCr_2O_4$ exhibits a transverse conical spin configuration, where spins are aligned in a conical plane with either clockwise or counterclockwise rotation [21–23]. This transverse conical spin configuration generates electric polarization through the multiferroic effect [24–26], where the sign of polarization corresponds to the direction of spin rotation [27]. Furthermore, using a multipole representation, the transverse conical spin configuration can be described as a magnetic toroidal dipole [28]. The multipole representation of spin configurations is useful for understanding the functional properties of noncollinear spin structures [29–37]. In contrast, when non-magnetic ions occupy the pyrochlore sublattice, spinel oxides tend to become antiferromagnetic due to the antiferromagnetic coupling between the T_d sites [38–41]. Moreover, some cobaltite spinels, such as $ZnCo_2O_4$ and $MnCo_2O_4$, also exhibit high electrical conductivity [42–44].

In the spinel structure, the ions at the T_d and O_h sites occupy Wyckoff positions that are multiples of $1/8$. In contrast, the Wyckoff position of oxygen is ideally $u = 0.375$ $(3/8)$, but in most compounds, it shifts away from the T_d ions. This displacement is referred to as the u-parameter, as shown in figure 1(b). As a result, four non-equivalent threefold rotation axes are generated around the oxygen-coordinated O_h site, specifically along the [111], [1$\bar{1}\bar{1}$], [$\bar{1}$1$\bar{1}$], and [$\bar{1}\bar{1}$1] directions, as shown in figure 1(c). The displacement of the u-parameter causes a shift in the oxygen positions surrounding the O_h site, aligning them closer to the rotational symmetry axes (see figure 1(b)). This leads to a slight distortion of the oxygen ions from the ideal octahedral arrangement [45], which consequently induces an additional crystal field potential. Due to the crystal symmetry, the degeneracy of the t_{2g} orbitals is further lifted, splitting them into a doublet and a singlet. The doublet is subsequently split by spin–orbit interaction (SOI). When the energy level of the doublet is higher than that of the singlet, a finite orbital angular momentum remains. This restoration of orbital angular momentum can induce significant magnetic anisotropy in some spinel oxides.

The orbital angular momentum induces significant magnetic anisotropy through SOIs [45, 46]. This effect is notably observed in cobalt ferrite ($CoFe_2O_4$) films containing Co^{2+} (d^7) ions at the O_h site [47–52]. By introducing a 3% tetragonal distortion through epitaxial strain, a large perpendicular magnetic anisotropy (PMA) of up to 6 MJ m^{-3} has been reported [53]. Moreover, since Co^{2+} is the origin of PMA, the magnetic anisotropy modulation was archived by doping Co to Fe_3O_4 [54, 55]. In addition to $CoFe_2O_4$, $NiCo_2O_4$ is another spinel oxide in which PMA has been observed due to epitaxial strain [56, 57]. The origin of PMA in $NiCo_2O_4$ films has been identified as the Co ions occupying the T_d sites [58–60]. Moreover, while $NiCo_2O_4$ exhibits PMA at room temperature, a spin reorientation into an easy-cone magnetic anisotropy (ECMA) has been reported at low temperatures [59]. Furthermore, this spin reorientation leads to a noncollinear spin structure characterized as a magnetic toroidal quadrupole (MTQ), which induces a novel Hall effect termed the quadrupole anomalous Hall effect (QuadAHE) [61].

In this review, we highlight recent advancements in epitaxial $NiCo_2O_4$ thin films, focusing on: (i) the tunability of anti-site defects through controlled fabrication conditions, (ii) the emergence of ECMA induced by these anti-site defects, (iii) the realization of a non-trivial spin structure characterized by MTQ order, driven by ECMA, (iv) novel magneto-transport phenomena arising from this non-trivial spin structure, and (v) this correlation between the non-trivial spin structure and the concept of altermagnetism.

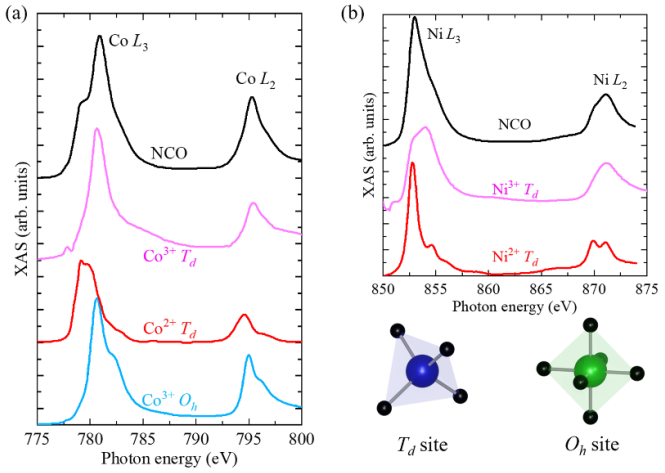

Figure 2. XAS spectrum of $NiCo_2O_4$ (NCO) around (a) Co and (b) Ni L-edges [56]. The reference spectra of Co are $EuCoO_3$ [70] (Co^{3+} at O_h), $YBaCo_3AlO_7$ [71] (Co^{2+} at T_d) and $YBaCo_4O_7$-$YBaCo_3AlO_7$ [71] (Co^{3+} at T_d), and that of Ni are NiO [72] (Ni^{2+} at O_h) and $LaNiO_3$ [73] (Ni^{3+} at O_h), respectively. Adapted from [56]. CC BY 4.0.

2. Fundamental properties of $NiCo_2O_4$

$NiCo_2O_4$ possesses an inverse spinel structure, which consists of diamond and pyrochlore sublattices [62]. The electronic states and magnetic structures of $NiCo_2O_4$ have been investigated using neutron diffraction, x-ray absorption spectroscopy (XAS), and x-ray magnetic circular dichroism (XMCD) spectroscopy experiments [56, 63–67]. From XAS spectra of $NiCo_2O_4$, as shown in figure 2, it can be expressed by the following structural formula:

$$\left(Co_x^{2+}Co_{1-x}^{3+}\right)_{\text{tet}}\left[Co^{3+}Ni_{1-x}^{2+}Ni_x^{3+}\right]_{\text{oct}}O_4^{2-} \quad (0<x<1), \quad (1)$$

where the subscripts 'tet' and 'oct' represent the T_d and O_h sites, respectively. This formula indicates that Co^{2+} (d^7; $S=3/2$) and Co^{3+} (d^6; $S=2$) occupy the T_d sites, while Ni^{2+} (d^8; $S=1$), Ni^{3+} (d^7; $S=1/2$), and Co^{3+} (d^6; $S=0$) occupy the O_h sites. The relationship between the spin state and the occupied site is summarized in figure 3. It also includes the anti-site defect of Ni^{3+} at the T_d site, which will be discussed in the following section. In addition, the mixed valence of cations contributes to the high conductivity of $NiCo_2O_4$ [68, 69].

The magnetic moment of $NiCo_2O_4$ arises from the valence-mixed sites, with Co ions occupying the T_d sites and Ni ions occupying the O_h sites. The XMCD measurements reveal that the T_d-site and the O_h-site are coupled antiferromagnetically, which induces a ferrimagnetic magnetization as determined in the magnetization hysteresis curve measured by vibrating sample magnetometer (VSM), as shown in figures 4(a) and (b). The XMCD measurements were performed by the total electron yield mode at an undulator beamline BL-16A, Photon Factory, High Energy Accelerator Research Organization (KEK), Tsukuba, Japan. From the perspective of the number of d-electrons at each site, the nominal saturation magnetization (M_S) is 2 μ_B/f.u., independent of the value of x. However,

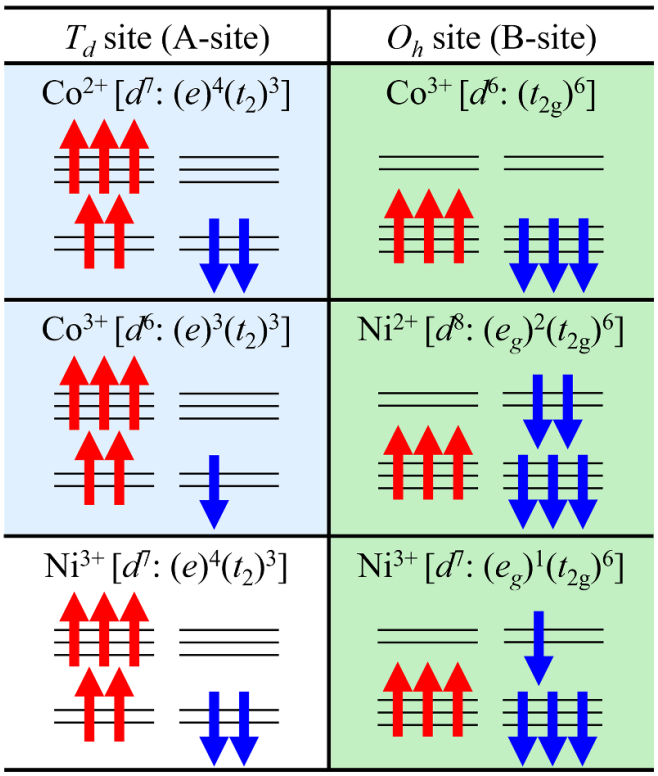

Figure 3. The relation between spin state and occupied site. The shad color corresponds to the occupied site in the ideal inverse spinel structure.

the value of x strongly depends on the fabrication method and conditions. Therefore, caution is required when comparing the properties of $NiCo_2O_4$ films fabricated by different methods or under different conditions, as such comparisons cannot be made straightforwardly or uniformly [74–76].

In thin-film form, due to finite-size effects [77–80], the Néel temperature and resistivity depend on the film thickness, as shown in figures 4(c) and (d) [57, 76]. Specifically, the Néel temperature gradually increases to approximately 400 K, and the resistivity reaches 1 mΩ cm. Moreover, an upturn appears at low temperatures in the temperature dependence of the resistivity, which can be attributed to weak localization [74, 81].

3. Cation distribution changes and anti-site defects caused by thin film shape

$NiCo_2O_4$ thin films have been fabricated using molecular beam epitaxy, pulsed laser deposition (PLD), and the sputtering technique [56, 57, 59, 82, 83]. Conductivity has been confirmed in all cases; however, its magnitude and temperature dependence vary depending on the fabrication method [75, 76, 84–88]. In addition to transport properties, magnetic properties also exhibit variations. These results suggest that the cation distribution is influenced by the fabrication conditions.

The inverse spinel structure can be represented as $B_{1-\delta}A_\delta[A_{1-\delta}B_{1+\delta}]O_4$. In an ideal inverse spinel structure, δ should be zero; however, in actual samples, δ is nonzero

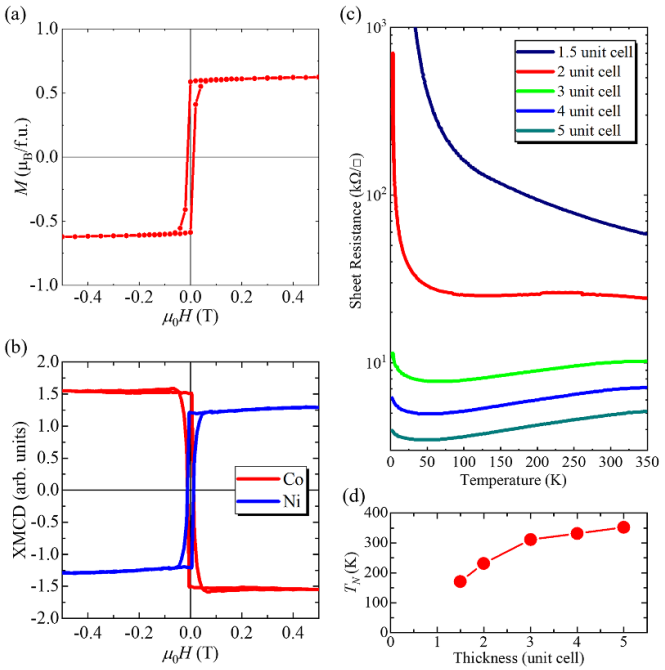

Figure 4. (a) Magnetization hysteresis loop of $NiCo_2O_4$ thin film. (b) Element-specific magnetic hysteresis loops by x-ray magnetic circular dichroism (XMCD) measured at L_3-edge of Co and Ni. Thickness dependence of (c) sheet resistance and (d) the Néel temperatures [76]. Reprinted from [76], with the permission of AIP Publishing.

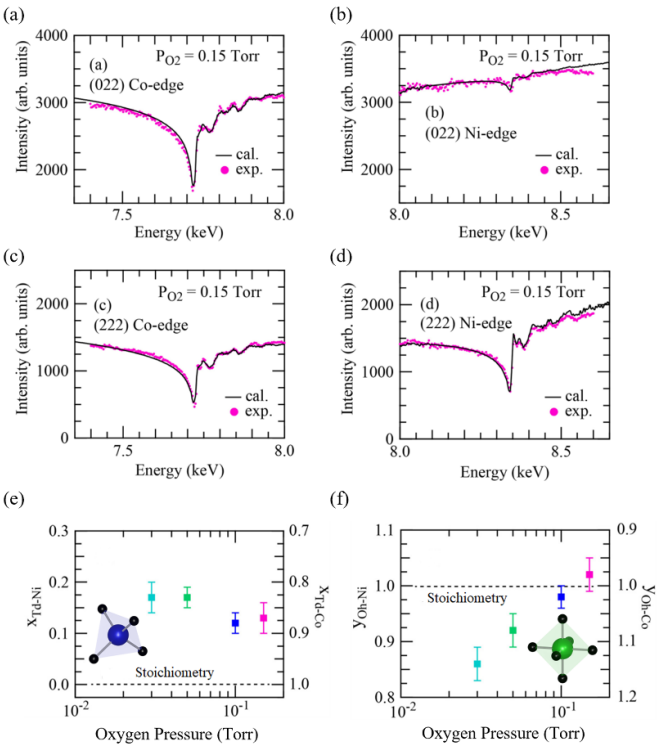

Figure 5. Incident x-ray energy dependence of anomalous x-ray scattering at (022) reflections around K-edge of (a) Co and (b) Ni ions, and at (222) reflections at K-edge of (c) Co and (d) Ni. (e) and (f) indicate the dependence of the cation distribution at the T_d and O_h sites on the oxygen pressure in the PLD method (P_{O_2}). Reprinted (figure) with permission from [83], Copyright (2020) by the American Physical Society.

due to the presence of anti-site defects. These anti-site defects can be quantitatively evaluated using the anomalous x-ray scattering technique [89–91]. The scattering intensity (I_{hkl}) is given by,

$$I_{hkl} = A|F_{hkl}|^2, \tag{2}$$

$$F_{hkl} = \sum_j \alpha_j f_j \exp\left[2\pi \mathrm{i}\left(hu + kv + lw\right)\right], \tag{3}$$

$$f_j = f_0 + f' + if'', \tag{4}$$

where A is a Lorentz's polarization factor, F_{hkl} is the structure factor at hkl reflection, (u, v, w) represents the Wyckoff position, and α_j is the jth site occupancy in the unit cell. The scattering factor f_j for the jth site atom is composed of the normal scattering factor f_0, and the real (imaginary) parts of the anomalous scattering correction factors f' (f'').

This formula indicates that when the incident x-ray energy is close to the absorption edges of each atom, the diffraction intensities are modified due to anomalous scattering correction factors. Since these factors reflect the elemental composition, the contributions of different elements to the diffraction can be estimated by reproducing the intensity modifications. In other words, a quantitative evaluation of anti-site defects can be achieved by performing anomalous scattering measurements on diffraction peaks corresponding to a single crystallographic site.

Since the T_d and O_h sites have different local symmetries, the contribution of each sublattice to diffraction varies. In particular, the (022) and (222) reflections originate from scattering by the cations at the T_d and O_h sites, respectively [83]. Figures 5(a)–(d) show the incident x-ray energy dependence of the (022) and (222) reflections around the K-edges of Co and Ni. The fitting results obtained using equation (2) agree well with the experimental data. Since the (022) reflections arise solely from the cations at the T_d site, anomalous scattering should not be observed in an ideal inverse spinel structure. Therefore, the small dip in figure 5(b) suggests that a minor fraction of Ni occupies the T_d site as an anti-site defect.

Figures 5(e) and (f) show the dependence of the cation distribution at the T_d and O_h sites on the oxygen pressure in the PLD method (P_{O_2}), as estimated by model calculations [83]. As P_{O_2} increases, the Ni composition at the O_h site increases, while that at the T_d site slightly decreases. Consequently, the overall composition of the $NiCo_2O_4$ films changes. This variation in site occupancy leads to changes in the magnetic properties of the $NiCo_2O_4$ films.

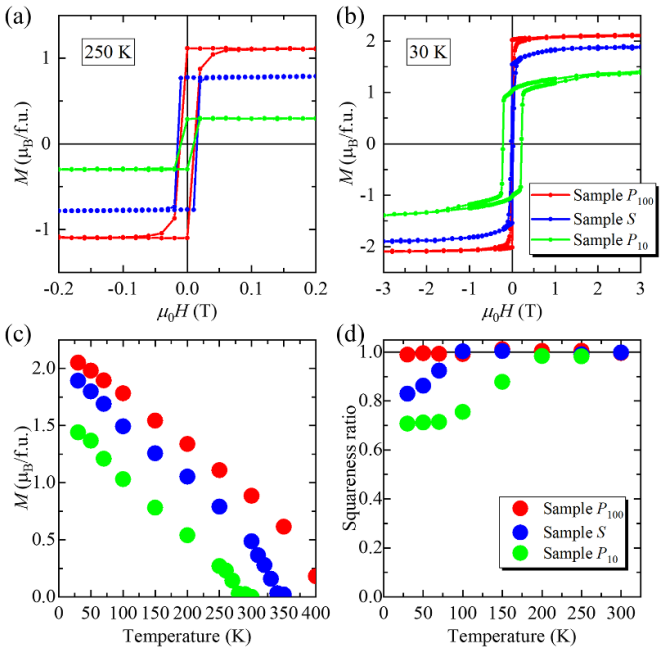

Figure 6. Magnetic properties of three $NiCo_2O_4$ thin films, Sample S, P_{100} and P_{10}. Magnetic hysteresis loop with $\mu_0 H \perp (001)$ plane of $NiCo_2O_4$ at (a) 250 K and (b) 30 K. (c) The temperature dependence of saturation magnetization and (d) dependence of the squareness ratio. Reprinted (figure) with permission from [59], Copyright (2021) by the American Physical Society.

4. The effect of anti-site defects for magnetic properties

Here, we discuss the magnetic properties of three epitaxial $NiCo_2O_4$ films with different fabrication conditions. One was fabricated by the reactive radio frequency magnetron sputtering, labeled as 'Sample S' , where the process temperature and working pressure were 300 °C and 1.3 Pa (Ar : O_2 = 10 sccm : 2.5 sccm), respectively. The others were fabricated by the PLD, labeled as 'Sample P_{100}' and 'Sample P_{10}', where the process temperature was 315 °C and the oxygen pressure of 10 mTorr for Sample P_{10} and 100 mTorr for Sample P_{100}, respectively [59]. The oxygen pressure and process temperature affect the $NiCo_2O_4$ film properties [59, 84]. All thin films were grown on single-crystal $MgAl_2O_4(001)$ substrates.

4.1. Magnetization

In most spinel magnets, the magnetic moments at the T_d and O_h sites are antiferromagnetically coupled. In the case of $NiCo_2O_4$, the spin state at the T_d site is in a high-spin state, while that at the O_h site is in a low-spin state, as shown in table 3, indicating that the spin moment of each cation depends on its occupied site. Therefore, the saturation magnetization varies depending on the ratio of anti-site defects.

Figures 6(a) and (b) show the magnetic hysteresis loops of three $NiCo_2O_4$ films fabricated under different conditions. At 250 K, as shown in figure 6(a), all films exhibit square-shaped hysteresis loops, while their saturation magnetization varies depending on the fabrication conditions. The squareness ratio, defined as the ratio of the remanent magnetization to the saturation magnetization, is 1.0 for all films. In contrast, at 30 K, as shown in figure 6(b), the hysteresis loop behavior varies among the samples. In Sample P_{100}, which closely approximates an ideal inverse spinel distribution, a square-shaped hysteresis loop similar to that at 250 K is observed. However, in Sample P_{10}, which deviates from the ideal structure, both the saturation magnetization and the squareness ratio decrease. Moreover, the coercivity increases as the squareness ratio decreases. Figures 6(c) and (d) show the temperature dependence of the saturation magnetization and the squareness ratio. As expected from the differences in cation distribution, both the saturation magnetization and the Néel temperature depend on the sample. In particular, the reduction in the squareness ratio suggests that the magnetic anisotropy may change at low temperatures.

4.2. Uniaxial magnetic anisotropy

The square-shaped hysteresis loops suggest the emergence of PMA. To investigate the effect of cation distribution differences on magnetic anisotropy, we examine the temperature dependence of magnetic anisotropy using the magneto–torque method [2, 92, 93]. The magneto–torque is defined as the derivative of the total energy with respect to the external magnetic field angles (θ and φ). It arises from the angular difference between the net magnetic moment and the external magnetic field.

In tetragonal crystal systems, the magnetic anisotropy energy (E_A) and magneto–torque for the ac-plane (L_θ) and ab-plane (L_φ) can be written as follows [2, 92]:

$$E_A = K_{u1}^{\text{eff}} \sin^2\theta + K_{u2} \sin^4\theta + K_3 \sin^4\theta \sin^2 2\varphi, \quad (5)$$

$$L_\theta \equiv -\partial_\theta E_A = -\left(K_{u1}^{\text{eff}} + K_{u2}\right) \sin 2\theta + \frac{1}{2} K_{u2} \sin 4\theta, \quad (6)$$

$$L_\varphi \equiv -\partial_\varphi E_A = -K_3 \sin 4\varphi\,, \quad (7)$$

where K_{u1}^{eff} and K_{u2} are the uniaxial magnetic anisotropy constants for the first- and second-order terms, respectively, and K_3 is the cubic anisotropy constant. Further, θ and φ represent the angles between the direction of the applied field and the c- and a-axes, respectively. The observed K_{u1}^{eff} consists of contributions from both magnetocrystalline anisotropy K_{u1} and shape anisotropy $\mu_0 M_S^2/2$, i.e.

$$K_{u1}^{\text{eff}} = K_{u1} - \frac{\mu_0 M_S^2}{2}. \quad (8)$$

The magnetic anisotropy constants allow us to determine the preferential directions of the net magnetization [2, 92]. These constants can be obtained from magneto–torque measurements using a setup in which the external field is rotated in the θ and φ directions, as shown in figures 7(a) and (b).

Figures 7(c) and (d) display the temperature evolution of L_θ and L_φ of Sample S. By fitting these torque curves using equations (6) and (7), the magnetic anisotropy constants can be

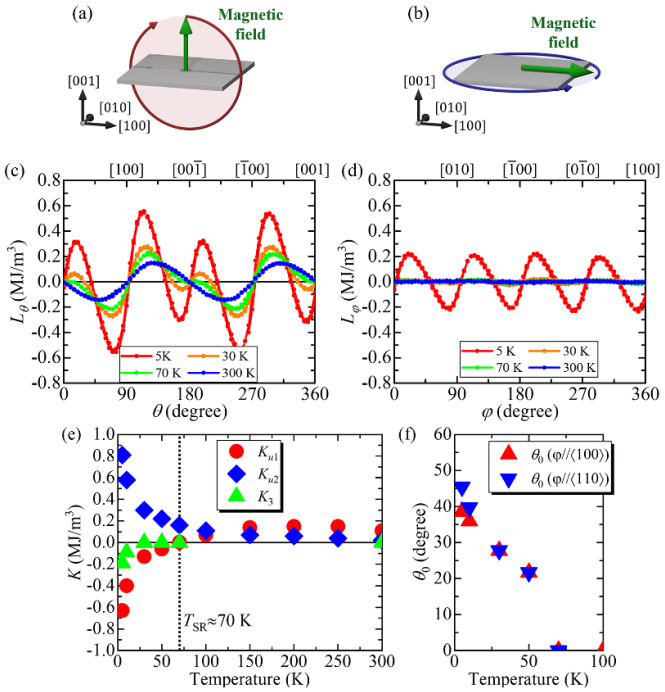

Figure 7. The schematic illustration of the magneto–torque measurement setup for (a) the θ direction and (b) the φ direction. Magneto–torque curves of (c) L_θ (in the *ac*-plane) and (d) L_φ (in the *ab*-plane) for Sample *S* at various temperatures. (e) The temperature dependence of the magnetic anisotropy constants for Sample *S*. (f) The cone angle for the two different directions, $\varphi \parallel \langle 100 \rangle$ and $\varphi \parallel \langle 110 \rangle$, estimated from equation (9). Reprinted (figure) with permission from [59], Copyright (2021) by the American Physical Society.

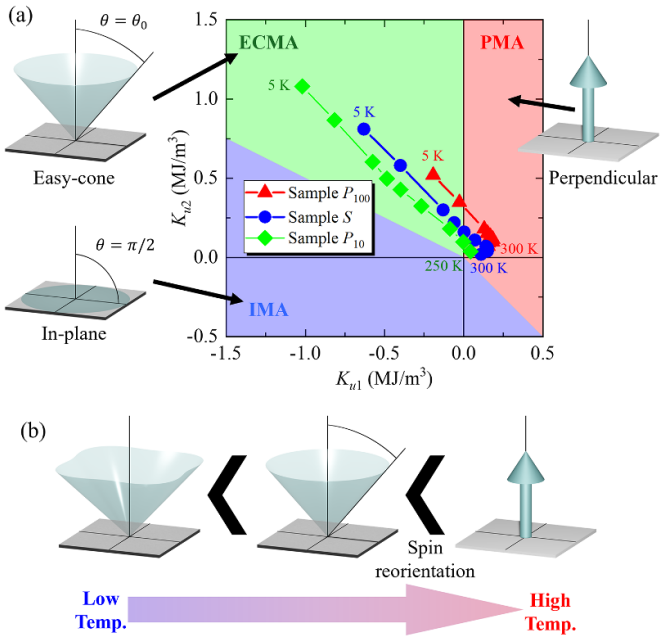

Figure 8. (a) The relationship between magnetic anisotropy constants at various temperatures ranging from 5 K to 300 K. The graph is color-coded according to the magnetic preferential direction. (b) A schematic illustration of the temperature dependence of magnetic preferential directions. Reprinted (figure) with permission from [59], Copyright (2021) by the American Physical Society.

determined. The magnetic easy axis can be estimated from the obtained magnetic anisotropy constants. When $K_{u1}^{\text{eff}} > 0$ and $-K_{u1}^{\text{eff}} > K_{u2}$, the magnetic preferential direction is perpendicular to the plane. In contrast, when $K_{u1}^{\text{eff}} < 0$ and $-K_{u1}^{\text{eff}} < 2K_{u2}$, the magnetic preferential direction lies within a conical plane. The cone angle θ_0, considering terms up to K_3 and defined with respect to the *c*-axis, can be expressed as

$$\sin\theta_0(\varphi) = \sqrt{\frac{-K_{u1}^{\text{eff}}}{2\left(K_{u2} + K_3 \sin^2 2\varphi\right)}}. \tag{9}$$

In other regions, the magnetic preferential direction lies within the in-plane direction. A correlation diagram between each coefficient and the magnetic preferential direction is shown in figure 8(a).

Figure 7(e) shows the estimated magnetic anisotropy constant in Sample *S*. Around room temperature, K_{u1} is positive, indicating that the magnetic easy axis is perpendicular to the plane. At 70 K, the sign of K_{u1} changes, and a positive K_{u2} emerges, implying a spin reorientation where the magnetic easy axis transitions from being perpendicular to lying within a conical plane. At even lower temperatures, K_3 emerges, indicating that the cone angles differ between $\varphi \parallel \langle 100 \rangle$ and $\varphi \parallel \langle 110 \rangle$, as shown in figure 7(f).

Figure 8(a) shows the sample dependence of the uniaxial magnetic anisotropy constants at various temperatures in the magnetic anisotropy phase diagram. All $NiCo_2O_4$ films exhibit PMA around room temperature, while an ECMA appears at lower temperatures. The spin reorientation temperature (T_{SR}), at which the magnetic anisotropy transitions from PMA to ECMA, depends on the fabrication conditions.

In summary, $NiCo_2O_4$ films exhibit PMA in the temperature range between the Néel temperature and T_{SR}. Below T_{SR}, the magnetic anisotropy transitions to ECMA, and at even lower temperatures, the conical shape becomes distorted into a four-fold symmetry due to the effect of K_3. The schematic illustration in figure 8(b) depicts the relationship between temperature and the magnetic preferential directions.

4.3. Electron theory for a magnetic anisotropy

A numerical calculation is performed to investigate the origin of ECMA within the framework of the cluster model [50, 51]. Due to the presence of anti-site disorders, there are eight possible cluster configurations, each consisting of four ions, i.e. Co^{2+}, Co^{3+}, Ni^{2+}, and Ni^{3+}, occupying either the T_d or O_h sites in $NiCo_2O_4$ films.

The electronic structure of the cluster was calculated using a tight-binding model for the 3*d*- and 2*p*-orbitals of the transition metal and oxygen ions, respectively, while incorporating SOI. We assumed that the 3*d* states of the Co and Ni ions are fully spin-polarized and that these ions possess local moments. The parameters for inter-site *p*–*d* hopping between the 3*d*-orbitals of a transition metal ion and the 2*p*-orbitals of the oxygen ions were obtained from Harrison's textbook [52,

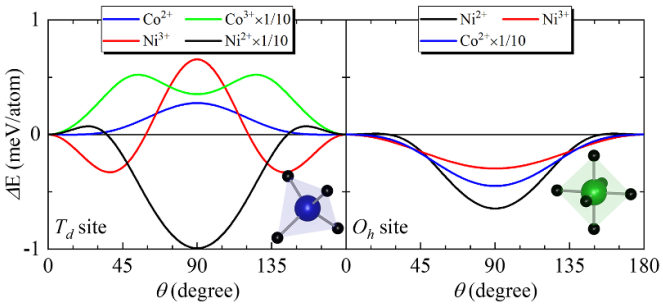

Figure 9. Calculated dependence of the magnetic moment on the angle $\Delta E(\theta)$ at (Left panel) T_d site, and (Right panel) O_h sites. Reprinted (figure) with permission from [59], Copyright (2021) by the American Physical Society.

94]. The ground-state energy was calculated by diagonalizing the Hamiltonian as a function of the magnetization direction. The lattice constant and Wyckoff position of $NiCo_2O_4$ were obtained from a previous report [64]. For details regarding the parameters used in the calculations, see [59].

Figures 9(a) and (b) show the angle-dependent energy of the magnetic moment (ΔE) at the T_d and O_h sites, respectively. Note that the calculation for Co^{3+} at the O_h site is excluded due to its low-spin state with $S=0$. The preferential spin direction of Co^{3+} at the T_d site is parallel to the c-axis, which is consistent with previous tight-binding calculations [58]. On the other hand, the preferential spin directions of Co^{2+} at the O_h site and Ni^{2+} at the T_d site lie within the ab-plane. The angle-dependent energy $\Delta E(\theta)$ of Ni^{3+} at the T_d site exhibits a large K_{u2}, with minima at approximately 45° and 135°. Therefore, the anti-site occupation of Ni^{3+} at the T_d site is the origin of ECMA. Supporting the calculation results, samples with a higher concentration of anti-site defects exhibit a higher T_{SR} and stronger ECMA.

5. ECMA and non-collinear spin structure

The anti-site $NiCo_2O_4$ thin film exhibits an unconventional anomalous Hall effect that depends on the current direction, termed the QuadAHE [61]. Here, we discuss the involvement of the conductivity and the noncollinear spin structure induced by the ECMA, which includes an extended magnetic multipole of the MTQ order.

5.1. Onsager's theorem for a resistivity tensor

According to the Neumann principle, the tensor of the physical property must remain invariant under the symmetry operations of the system [95, 96]. The resistivity tensor (ρ_{ij}) of magnetically ordered materials is expressed as $E_i = \rho_{ij}(\boldsymbol{H},\boldsymbol{\Sigma})J_j$, where $\boldsymbol{E}$, $\boldsymbol{J}$, $\boldsymbol{H}$, and $\boldsymbol{\Sigma}$ represent the electric field, applied current, external magnetic field, and spin configuration, respectively [97–99]. Applying the time-reversal operation $\mathcal{T}$ changes the signs of magnetic field and magnetic structure, i.e. $\mathcal{T}\boldsymbol{H} = -\boldsymbol{H}$ and $\mathcal{T}\boldsymbol{\Sigma} = -\boldsymbol{\Sigma}$. Consequently, Onsager's theorem provides the reciprocal relation in the resistivity tensor [100]:

$$\rho_{ij}(\boldsymbol{H},\boldsymbol{\Sigma}) = \mathcal{T}\rho_{ji}(\boldsymbol{H},\boldsymbol{\Sigma}) = \rho_{ji}(-\boldsymbol{H},-\boldsymbol{\Sigma}). \tag{10}$$

Considering Hall effects as an odd function of H_z and M_z, we obtain the relation:

$$\rho_{xy}(H_z,M_z) = -\rho_{yx}(H_z,M_z), \tag{11}$$

which indicates that when $\boldsymbol{J} \parallel x\ (y)$, the induced electric field $\boldsymbol{E}$ aligns along $y\ (-x)$ in the presence of H_z and M_z. Since equation (11) suggests that rotational symmetry is preserved in the plane normal to $\boldsymbol{H}$ and $\boldsymbol{M}$, the Hall voltage should be independent of the direction of $\boldsymbol{J}$. Therefore, the conventional Hall effect, an odd function of the transverse resistance component for H_z and M_z, remains isotropic for different current directions from Onsager's theorem [98]. However, in this section, we demonstrate an unconventional anisotropic Hall effect. Although this behavior appears to violate Onsager's theorem, it can be explained consistently by assuming that the magnetic multipole component of the MTQ remains unchanged upon the reversal of M_z.

5.2. QuadAHE

The anisotropic Hall effects were demonstrated in epitaxial $NiCo_2O_4(001)$ films on $MgAl_2O_4(001)$ substrates. We present experimental evidence for the anisotropic Hall effect measured at 5 K. Before low-temperature measurements, the sample was cooled from room temperature under a low positive or negative magnetic field ($\mu_0 H_{FC} = \pm 0.1$ T), applied nearly perpendicular to the film plane. Figures 10(a)–(d) show the dependence of the Hall effect on the applied magnetic field $\boldsymbol{H} \parallel [001]$, with varying applied current directions. The odd function Hall resistivities ρ_{ij}^{O} ($i,j = x:[100]$, $y:[010]$) were extracted by anti-symmetrizationlysis. The Hall effects measured after the field cooling (FC) procedure with positive and negative H_{FC} are denoted as ρ_{ij}^{O+} and ρ_{ij}^{O-}, respectively, as shown in figures 10(a)–(d). Compared with figures 10(a)–(d), we find that ρ_{xy}^{O+} and $-\rho_{yx}^{O-}$ ($-\rho_{yx}^{O+}$ and ρ_{xy}^{O-}) are in good agreement with each other. Thus, the unconventional anisotropic response depends on both the applied current and FC directions.

Here we consider the decomposition of the Hall response into isotropic and anisotropic components for the applied current direction. Figures 10(a)–(d) suggest that only the anisotropic component depends on the FC direction. Thus, the anisotropic and isotropic components can be extracted by taking the difference and average of the Hall resistivities measured under opposite FC conditions. Figures 10(e) and (f) show the derived anisotropic component, $\rho_{Quad} = \rho_{xy}^{O+} - \rho_{xy}^{O-}$, and the isotropic component, $\rho_{AHE} = (\rho_{xy}^{O+} + \rho_{xy}^{O-})/2$, respectively. Moreover, when the current direction changes from $\boldsymbol{J} \parallel [100]$ to $\boldsymbol{J} \parallel [010]$, the sign of ρ_{Quad} is reversed. This indicates the anisotropic Hall effect follows a $\cos 2\varphi$ dependence on the current angle φ measured from the [100] axis. In the case of zero-field cooling, the anisotropic Hall effect cancels out and the resulting curve matches ρ_{AHE}. This suggests

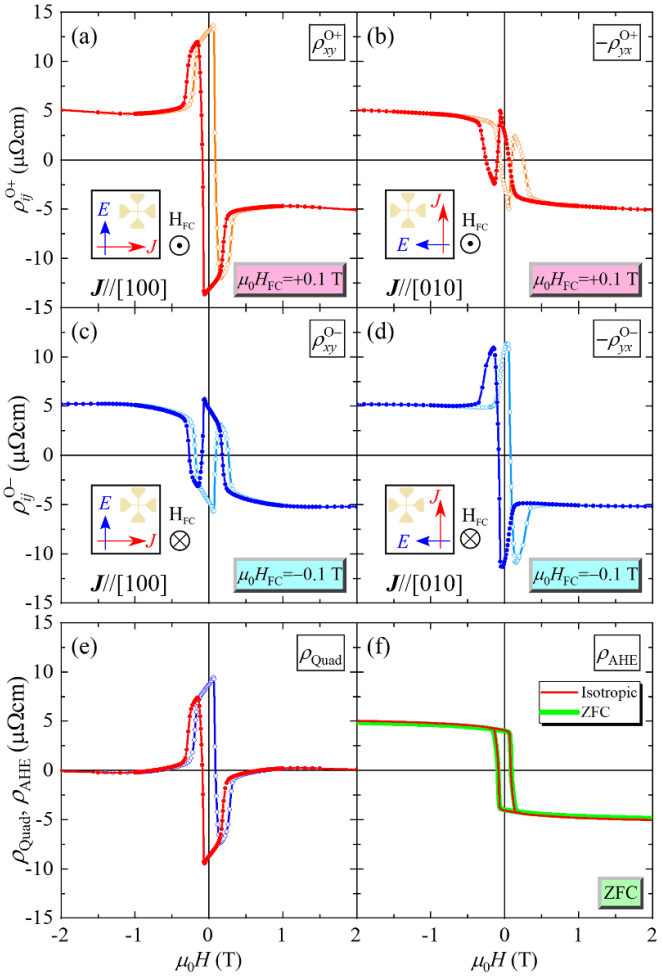

Figure 10. Magnetic field dependence of antisymmetric component of transverse resistivity with changing applied current direction ($\boldsymbol{J}$) and cooling field ($\mu_0 H_{FC}$). (a) $\boldsymbol{J} \parallel [100]$ and (b) $\boldsymbol{J} \parallel [010]$ with $\mu_0 H_{FC} = +0.1$ T. (c) $\boldsymbol{J} \parallel [100]$ and (b) $\boldsymbol{J} \parallel [010]$ with $\mu_0 H_{FC} = -0.1$ T. The open and closed symbols correspond to the sweep direction of the measurement field. The dark colors (red and blue) imply positive to negative, and light colors (orange and light blue) are negative to positive. The extracted (e) anisotropic and (f) isotropic components from the difference and average of (a) and (c), respectively. Reproduced from [61]. CC BY 4.0.

that the cooling process does not influence the M_z–H curve, as shown in figure 10(f). To generalize the above results, the series of Hall resistivities can be expressed as

$$\rho^{O\pm}(\varphi) = \rho^{OI} \pm \rho^{OA} \cos 2\varphi \tag{12}$$

where ρ^{OI} and ρ^{OA} represent the isotropic and anisotropic components of the Hall effect, respectively. The plus/minus sign corresponds to the sign of the cooling magnetic field. These results suggest that the field cooling procedure induces the single domain of a non-trivial spin structure.

5.3. Symmetry analysis and cluster magnetic multipole

Only the isotropic component appears in the high-field region ($|\mu_0 H| > 2$ T), indicating that the spins are collinearly aligned. This corresponds to the magnetic point group $4/mm'm'$. In contrast, in the low field region ($|\mu_0 H| < 1$ T), where the anisotropic component emerges, the observed $\cos 2\varphi$ dependence suggests a magnetic structure with $C_4\mathcal{T}$ symmetry by way of in-plane antiferromagnetic configuration. Such a structure can be realized in a pyrochlore lattice formed by the spinel O_h site. The pyrochlore lattice supports 12 orthonormal irreducible magnetic structures, characterized by extended multipoles respecting spatial inversion symmetry. These include three magnetic dipoles, four magnetic octupoles, and five MTQ moments (see [32, 101]). Among these, the $C_4\mathcal{T}$ symmetry is preserved in both T_u $(4'/mmm')$ and T_{xy} $(4'/mm'm)$. Moreover, since the $\cos 2\varphi$ response suggests the presence of the (110) mirror symmetry combined with $\mathcal{T}$, the MTQ T_u $(4'/mmm')$ provides a reasonable explanation for the experimental results. Next, let us consider the construction of a conical spin structure from the MTQ T_u, as $NiCo_2O_4$ films exhibit exchange coupling-mediated anisotropy (ECMA). When the MTQ T_u is combined with the magnetic octupole M_{xyz}, the z-component contributions cancel out, forming an in-plane antiferromagnetic spin structure, denoted as $\tilde{T}_u$ $(4'/mmm')$ [61]. Finally, a conical spin structure is established by incorporating a magnetic dipole component along the z-direction, as illustrated in figure 11. These considerations suggest that the QuadAHE originates from the MTQ.

5.4. Magneto-transport model for QuadAHE

$\mathcal{T}$-odd magnetic orders with spatial inversion symmetry induce symmetric band dispersions with spin splitting [33]. The $\mathcal{T}$-odd MTQ T_u moment in the $4'/mmm'$ magnetic point group leads to quadrupole-type spin splitting, similar to that observed in d-wave altermagnets. To investigate magnetotransport phenomena, we consider a minimal model Hamiltonian for the conical magnetic order of MTQ $\tilde{T}_u$, given by

$$\mathcal{H} = \sum_{\boldsymbol{k}\sigma\sigma'} \left[\frac{\hbar^2}{2m} \left(\boldsymbol{k}^2 \sigma_0 + 2\tilde{t}_u k_x k_y \sigma_z \right) + m_z \sigma_z \right] c^\dagger_{\boldsymbol{k}\sigma} c_{\boldsymbol{k}\sigma'} \tag{13}$$

where $c^\dagger_{\boldsymbol{k}\sigma}$ ($c_{\boldsymbol{k}\sigma}$) denotes the creation (annihilation) operator of an electron with wave vector $\boldsymbol{k}$ and spin σ_i $(i = 0, x, y, z)$ [33]. Here, m_z and $\tilde{t}_u$ represent the molecular fields arising from the magnetic dipole M_z and the MTQ $\tilde{T}_u$ orders, respectively. For simplicity, we consider only the $k_z = 0$ plane. The term $k_x k_y \sigma_z$ describes the quadrupole-type spin splitting due to the $C_4\mathcal{T}$ symmetry. Using the Boltzmann transport equation, the charge conductivity is obtained as

$$\begin{pmatrix} \sigma_\parallel \\ \sigma_\perp \end{pmatrix} = \sigma_D \begin{pmatrix} \bar{n}\left(1 + \tilde{t}_u^2\right) + 2\Delta n \tilde{t}_u \sin 2\varphi \\ 2\Delta n \tilde{t}_u \cos 2\varphi \end{pmatrix}, \tag{14}$$

where $\bar{n}$ and Δn represent the average and difference in electron numbers for up and down spins, respectively. The $\cos 2\varphi$ dependence reproduces the angular dependence of the observed QuadAHE. Since both Δn and $\tilde{t}_u$ are $\mathcal{T}$-odd, QuadAHE is a $\mathcal{T}$-even phenomenon. If $\tilde{t}_u$ remains unchanged upon the reversal of M_z, meaning that the in-plane antiferromagnetic structure is preserved. At the same time, only

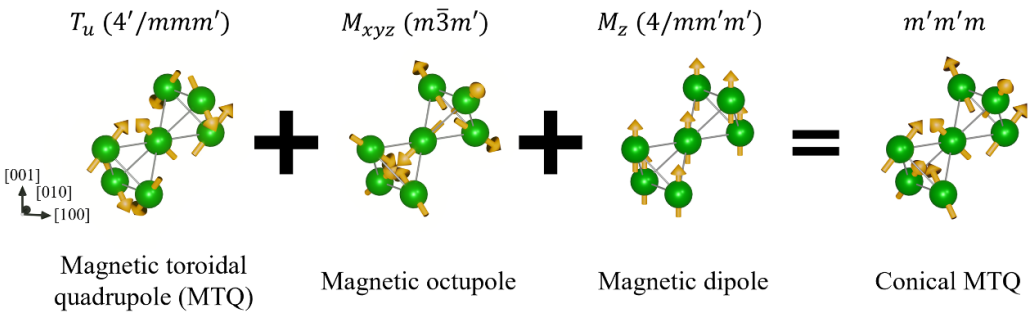

Figure 11. The formation of the conical spin structure from the bases of cluster multipole theory. The conical spin structure can be formed from the sum of MTQ (4′/mmm′) and magnetic octupole (m3̄m′) and magnetic dipole (4/mm′m′). Reproduced from [61]. CC BY 4.0.

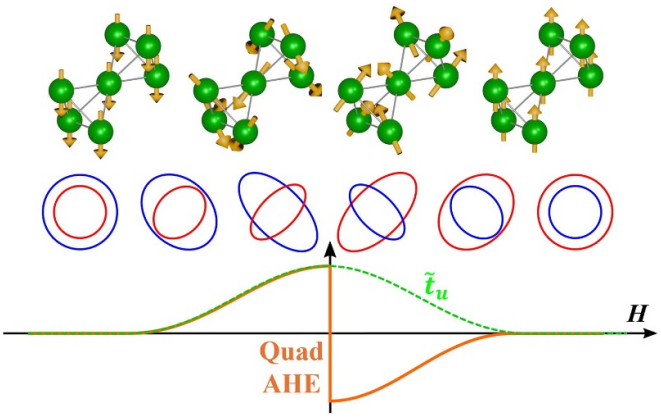

Figure 12. Schematic image of the applied field dependence of the spin structure and expected Fermi surface, and assumed the order parameters dependence. Reproduced from [61]. CC BY 4.0.

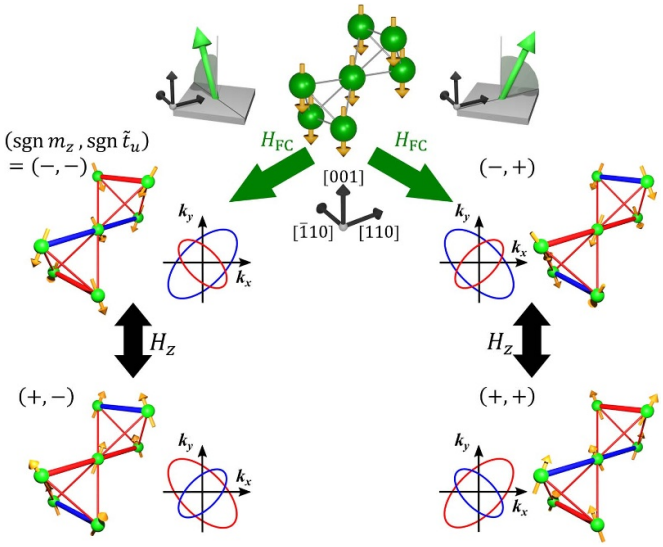

Figure 13. The spin structure and electronic band structure changes of the four degenerated states by the cooling magnetic field (H_{FC}) and measurement field (H_z). Reproduced from [61]. CC BY 4.0.

the perpendicular ferromagnetic component M_z is reversed, QuadAHE exhibits an antisymmetric response concerning M_z.

Figure 12 illustrates schematics of the electronic bands and spin structure modified by the external magnetic field. At high magnetic field regions, the band dispersion is isotropic due to the collinear ferrimagnetic structure. In contrast, at low magnetic field regions, the MTQ $\tilde{T}_u$ conical spin structure induces the anisotropic d-wave spin splitting. Assuming symmetric MTQ $\tilde{T}_u$ with respect to M_z, only the band sizes of the up and down spins change, contributing to the reversal of QuadAHE. Consequently, the anisotropic Hall effect is observed without violating Onsager's theorem.

5.5. Magnetic domain control of extended MTQ moment by magnetic-field cooling

From the previous transport model, the conical MTQ possesses four degenerate states; $(\mathrm{sgn}\ m_z, \mathrm{sgn}\ \tilde{t}_u) = (+,+),(+,-),(-,+),(-,-)$. The complete sign inversion of QuadAHE by H_{FC} indicates the MTQ domain can be controlled via the FC procedure. The selection of the MTQ state through magnetic field cooling can be interpreted by the Dzyaloshinskii–Moriya (DM) interactions [102, 103]. In the pyrochlore structure, a nonzero DM vector exists on bonds between the O_h-site ions [104, 105]. Figure 13 illustrates the DM interaction energy in the four MTQ conical magnetic order. The radii and colors correspond to the magnitude and sign of the energy. The four conical MTQ states remain energetically degenerate if the conical axis is parallel to the z-axis. However, when the DM vectors exhibit non-equivalent magnitudes due to the epitaxial strain, the degeneracy is lifted when the conical axis is tilted toward the $\langle 110 \rangle$ axes. The most stable MTQ conical state is uniquely determined by the sign of M_z and the tilting direction ([110] or [1$\bar{1}$0]). Thus, a single MTQ domain is realized when a slightly tilted H_{FC} is applied during the magnetic structure transition upon cooling. The sign of this domain is determined by both the tilted direction and the sign of H_z. In the actual experiments, H_{FC} is applied primarily along the z-direction. However, a small in-plane component remains, leading to a tilted H_{FC}.

5.6. d-wave spin splitting induced by MTQ in a spinel structure

We discuss the relationship between the MTQ spin structure and altermagnetism [106–117]. As discussed in the previous

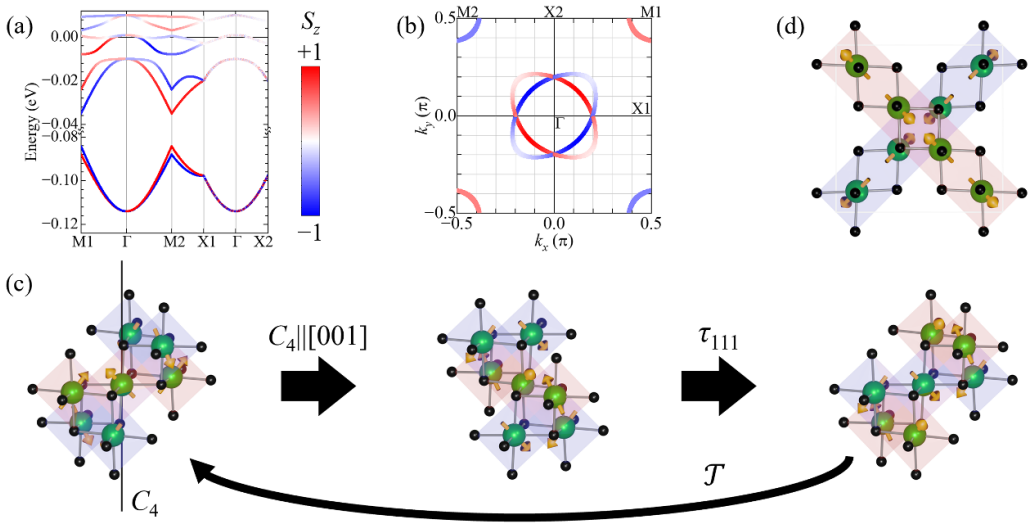

Figure 14. (a) The band dispersion in the k_xk_y-plane and (b) the Fermi surface with the spin structure of MTQ(T_u). (c) Spin rotation operation of an octahedron of pyrochlore sublattices. The red and blue shadings correspond to the sign of σ_z. (d) The top view of MTQ spin structure with the oxygen octahedron.

section, a characteristic Fermi surface, where the up- and down-spin states are split in the k_xk_y-plane, is predicted for the MTQ spin structure [33, 37]. To investigate this, we calculate the band dispersion of the pyrochlore sublattice, incorporating the MTQ spin structure. The Hamiltonian of the tight-binding model is given by

$$\mathcal{H}_k = -t_0 \sum_{\langle i,j \rangle} \boldsymbol{c}_i^\dagger \boldsymbol{c}_j + h.c. - \sum_j c_j^\dagger \left(B_j \cdot \sigma\right) c_j \qquad (15)$$

where t_0 and $\boldsymbol{\sigma}$ are the spin-independent hopping parameter and the Pauli matrices, $\langle i,j \rangle$ indicates all pairs of nearest-neighboring sites, $\boldsymbol{c}_i^\dagger = (c_{i\uparrow}^\dagger, c_{i\downarrow}^\dagger)$ is the creation operator for up- and down-spin electrons, and $\boldsymbol{B}$ is an effective magnetic field.

Figures 14(a) and (b) display the band dispersion in the k_xk_y-plane and the Fermi surface with the spin structure of T_u. As expected, a characteristic in-plane spin splitting, similar to that of a d-wave altermagnet, emerges. It is noteworthy that the presence of non-magnetic ions is important for altermagnetism. In contrast, the characteristic present band structure is realized only by the magnetic ions.

Next, we consider the oxygen atoms surrounding the pyrochlore sublattices in spinel oxide with the MTQ spin structure. The shading color of the octahedral is distinguished by focusing on the z-components (S_z) of the magnetic ions in the octahedra. Specifically, those with positive S_z are colored red, and those with negative S_z are colored blue. We now consider the symmetry operations. A four-fold crystal rotation (C_4) around the [001] axis combined with a half-unit cell translation along the [111] axis, as illustrated in figure 14(c), interchanges the red and blue octahedra. Therefore, when the MTQ spin structure is realized in the pyrochlore sublattice of the spinel lattice, it manifests as a d-wave altermagnet. In other words, the QuadAHE is the same phenomenon as the anisotropic transverse spin current in the d-wave altermagnet [107, 118]. It can be understood as being generated by the electric current due to the out-of-plane spin component of MTQ conical magnetic structure. This behavior can be attributed to the u-parameter, which induces octahedral distortion in different directions depending on their colors, as shown in figure 14(d).

6. Conclusion

In this review, we introduced recent advances in the tunable magnetic properties of epitaxial $NiCo_2O_4$ films and their characteristic features. $NiCo_2O_4$ possesses an inverse spinel structure and exhibits ferrimagnetism with high electrical conductivity. Moreover, it has attracted significant interest in spintronics due to its half-metallicity and PMA. Additionally, its properties can be tailored by adjusting the fabrication conditions.

The anti-site defects in $NiCo_2O_4$ are quantitatively evaluated using the anomalous scattering technique. These defects strongly influence the magnetic properties, particularly the magnetic anisotropy, which is highly dependent on the cation distribution. This dependence induces spin reorientation, where the magnetic anisotropy transitions from PMA to ECMA at low temperatures. As a result, the preferred magnetic direction changes from being perpendicular to the plane to lying within a conical plane.

The spin reorientation gives rise to a nontrivial noncollinear spin structure, which can be described as a MTQ within the framework of extended multipole representation. This conical spin structure exhibits the unconventional Hall effect, termed the QuadAHE, which depends on the applied current direction. At first glance, this novel magneto-transport phenomenon appears to violate Onsager's reciprocal theorem. However, by considering the interplay between the MTQ and the magnetic dipole, we can resolve this apparent contradiction. The MTQ induces spin splitting in the in-plane directions, exhibiting similarities to d-wave altermagnets. Furthermore, when considering the oxygen atoms surrounding the pyrochlore sublattices, the MTQ spin structure satisfies the symmetry conditions

of altermagnetism due to the *u*-parameter-induced octahedral distortions.

These advances are expected to pave the way for new emergent properties with potential applications in spintronic devices, such as multi-valued memory devices utilizing the electron nematic state. Furthermore, they may open a new research avenue into Hall effects originating from extended magnetic multipoles.

Data availability statement

All data that support the findings of this study are included within the article (and any supplementary files).

Acknowledgments

The authors thank H Yanagihara for the productive discussion. This work was performed under the approval of the Photon Factory Program Advisory Committee (Proposals Nos. 2017G602, 2016S2-005 and 2021S2-004). This project is partly supported by the Japan Society for the Promotion of Science (JSPS) KAKENHI (19H04399, 24K03205, 24H01685, and 24K17603). This work was supported by MEXT Quantum Leap Flagship Program (MEXT Q-LEAP) Grant No. JPMXS0118068681. This work is also partially supported by CREST(JPMJCR1861 and JPMJCR2435), Japan Science and Technology Agency (JST). H K acknowledges partly support of Grant-in-Aid for JSPS Fellows (22J00871).

ORCID iD

Hiroki Koizumi https://orcid.org/0000-0002-2293-9428

References

[1] Dionne G 2010 *Magnetic Oxides* (Springer US) (available at: https://books.google.co.jp/books?id=SgCzSYH8-bIC)
[2] Chikazumi S and Graham C D 1997 *Physics of Ferromagnetism* (Oxford University Press)
[3] Price G D, Price S L and Burdett J K 1982 *Phys. Chem. Miner.* **8** 69
[4] Farshidfar F, Lapolla M and Ghandi K 2024 *Mater. Today Chem.* **36** 101929
[5] Anderson P W 1956 *Phys. Rev.* **102** 1008
[6] Lyons D H, Kaplan T A, Dwight K and Menyuk N 1962 *Phys. Rev.* **126** 540
[7] Yafet Y and Kittel C 1952 *Phys. Rev.* **87** 290
[8] Kaplan T A 1959 *Phys. Rev.* **116** 888
[9] Kaplan T A 1960 *Phys. Rev.* **119** 1460
[10] Kaplan T A, Dwight K, Lyons D and Menyuk N 1961 *J. Appl. Phys.* **32** S13
[11] Ruff A, Wang Z, Zherlitsyn S, Wosnitza J, Krohns S, Krug von Nidda H-A, Lunkenheimer P, Tsurkan V and Loidl A 2019 *Phys. Rev. B* **100** 014404
[12] Sundaresan A and Ter-Oganessian N V 2021 *J. Appl. Phys.* **129** 060901
[13] Taguchi Y, Oohara Y, Yoshizawa H, Nagaosa N and Tokura Y 2001 *Science* **291** 2573
[14] Hastings J M and Corliss L M 1962 *Phys. Rev.* **126** 556
[15] Tomiyasu K and Kagomiya I 2004 *J. Phys. Soc. Japan* **73** 2539
[16] Bramwell S T *et al* 2001 *Phys. Rev. Lett.* **87** 047205
[17] Lee S-H, Broholm C, Ratcliff W, Gasparovic G, Huang Q, Kim T H and Cheong S-W 2002 *Nature* **418** 856
[18] Yamada Y, Kamazawa K and Tsunoda Y 2002 *Phys. Rev. B* **66** 064401
[19] Kamazawa K, Tsunoda Y, Kadowaki H and Kohn K 2003 *Phys. Rev. B* **68** 024412
[20] Kadowaki H, Ishii Y, Matsuhira K and Hinatsu Y 2002 *Phys. Rev. B* **65** 144421
[21] Tomiyasu K, Fukunaga J and Suzuki H 2004 *Phys. Rev. B* **70** 214434
[22] Yamasaki Y, Miyasaka S, Kaneko Y, He J-P, Arima T and Tokura Y 2006 *Phys. Rev. Lett.* **96** 207204
[23] Singh K, Maignan A, Simon C and Martin C 2011 *Appl. Phys. Lett.* **99** 172903
[24] Katsura H, Nagaosa N and Balatsky A V 2005 *Phys. Rev. Lett.* **95** 057205
[25] Nagaosa N and Tokura Y 2012 *Phys. Scr.* **2012** 014020
[26] Tokura Y, Seki S and Nagaosa N 2014 *Rep. Prog. Phys.* **77** 076501
[27] Yamasaki Y, Sagayama H, Goto T, Matsuura M, Hirota K, Arima T and Tokura Y 2007 *Phys. Rev. Lett.* **98** 147204
[28] Spaldin N A, Fiebig M and Mostovoy M 2008 *J. Phys.: Condens. Matter* **20** 434203
[29] Hayami S and Kusunose H 2018 *J. Phys. Soc. Japan* **87** 033709
[30] Kusunose H, Oiwa R and Hayami S 2020 *J. Phys. Soc. Japan* **89** 104704
[31] Hayami S, Yanagi Y and Kusunose H 2020 *Phys. Rev. B* **102** 144441
[32] Suzuki M-T, Nomoto T, Arita R, Yanagi Y, Hayami S and Kusunose H 2019 *Phys. Rev. B* **99** 174407
[33] Hayami S, Yatsushiro M, Yanagi Y and Kusunose H 2018 *Phys. Rev. B* **98** 165110
[34] Yatsushiro M, Kusunose H and Hayami S 2021 *Phys. Rev. B* **104** 054412
[35] Kusunose H, Oiwa R and Hayami S 2023 *Phys. Rev. B* **107** 195118
[36] Kirikoshi A and Hayami S 2023 *Phys. Rev. B* **107** 155109
[37] Hayami S and Yatsushiro M 2022 *J. Phys. Soc. Japan* **91** 063702
[38] Roth W 1964 *J. Phys. Chem. Solids* **25** 1
[39] Suzuki T, Nagai H, Nohara M and Takagi H 2007 *J. Phys.: Condens. Matter* **19** 145265
[40] Bhowmik R N and Ranganathan R 2007 *Phys. Rev. B* **75** 012410
[41] Dutta P, Seehra M S, Thota S and Kumar J 2007 *J. Phys.: Condens. Matter* **20** 015218
[42] Perkins J D *et al* 2011 *Phys. Rev. B* **84** 205207
[43] Zakutayev A, Paudel T R, Ndione P F, Perkins J D, Lany S, Zunger A and Ginley D S 2012 *Phys. Rev. B* **85** 085204
[44] Zaouali A, Dhahri A, Boughariou A, Dhahri E, Barillé R, Costa B F O and Khirouni K 2021 *J. Mater. Sci., Mater. Electron.* **32** 1221
[45] Tachiki M 1960 *Prog. Theor. Phys.* **23** 1055
[46] Slonczewski J C 1958 *Phys. Rev.* **110** 1341
[47] Niizeki T, Utsumi Y, Aoyama R, Yanagihara H, Inoue J, Yamasaki Y, Nakao H, Koike K and Kita E 2013 *Appl. Phys. Lett.* **103** 162407
[48] Tanaka M A, Harada K, Takemura M, Mibu K and Inoue J 2014 *J. Appl. Phys.* **115** 17C101
[49] Tainosho T, Inoue J-I, Sharmin S, Takeguchi M, Kita E and Yanagihara H 2019 *Appl. Phys. Lett.* **114** 092408
[50] Inoue J, Niizeki T, Yanagihara H, Itoh H and Kita E 2014 *AIP Adv.* **4** 027111
[51] Inoue J, Yanagihara H and Kita E 2014 *Mater. Res. Express* **1** 046106

[52] Inoue J 2015 *J. Phys. D: Appl. Phys.* **48** 445005
[53] Onoda H, Sukegawa H, Inoue J and Yanagihara H 2021 *Adv. Mater. Interfaces* **8** 2101034
[54] Okabayashi J, Tanaka M A, Morishita M, Yanagihara H and Mibu K 2022 *Phys. Rev. B* **105** 134416
[55] Morishita M, Ichikawa T, Tanaka M A, Furuta M, Mashimo D, Honda S, Okabayashi J and Mibu K 2023 *Phys. Rev. Mater.* **7** 054402
[56] Bitla Y *et al* 2015 *Sci. Rep.* **5** 15201
[57] Chen X, Zhang X, Han M-G, Zhang L, Zhu Y, Xu X and Hong X 2019 *Adv. Mater.* **31** 1805260
[58] Mellinger C, Waybright J, Zhang X, Schmidt C and Xu X 2020 *Phys. Rev. B* **101** 014413
[59] Koizumi H, Suzuki I, Kan D, Inoue J, Wakabayashi Y, Shimakawa Y and Yanagihara H 2021 *Phys. Rev. B* **104** 014422
[60] Koizumi H and Yanagihara H 2024 *J. Magn. Soc. Japan* **48** 108
[61] Koizumi H, Yamasaki Y and Yanagihara H 2023 *Nat. Commun.* **14** 8074
[62] Holgersson S and Karlsson A 1929 *Z. Anorg. Allg. Chem.* **183** 384
[63] Knop O, Reid K I G, Sutarno and Nakagawa Y 1968 *Can. J. Chem.* **46** 3463
[64] Battle P, Cheetham A and Goodenough J 1979 *Mater. Res. Bull.* **14** 1013
[65] Lenglet M, Guillamet R, Dürr J, Gryffroy D and Vandenberghe R 1990 *Solid State Commun.* **74** 1035
[66] Marco J, Gancedo J, Gracia M, Gautier J, Ríos E and Berry F 2000 *J. Solid State Chem.* **153** 74
[67] Kan D, Mizumaki M, Kitamura M, Kotani Y, Shen Y, Suzuki I, Horiba K and Shimakawa Y 2020 *Phys. Rev. B* **101** 224434
[68] King W and Tseung A 1974 *Electrochim. Acta* **19** 485
[69] Windisch C, Exarhos G, Ferris K, Engelhard M and Stewart D 2001 *Thin Solid Films* **398-399** 45
[70] Hu Z *et al* 2004 *Phys. Rev. Lett.* **92** 207402
[71] Hollmann N, Hu Z, Valldor M, Maignan A, Tanaka A, Hsieh H H, Lin H-J, Chen C T and Tjeng L H 2009 *Phys. Rev. B* **80** 085111
[72] Tanaka A and Jo T 1994 *J. Phys. Soc. Japan* **63** 2788
[73] Kitamura M *et al* 2019 *Phys. Rev. B* **100** 245132
[74] Silwal P, Miao L, Hu J, Spinu L, Ho Kim D and Talbayev D 2013 *J. Appl. Phys.* **114** 103704
[75] Kan D, Xie L and Shimakawa Y 2021 *Phys. Rev. B* **104** 134407
[76] Chen X, Wu Q, Zhang L, Hao Y, Han M-G, Zhu Y and Hong X 2022 *Appl. Phys. Lett.* **120** 242401
[77] Huang F, Kief M T, Mankey G J and Willis R F 1994 *Phys. Rev. B* **49** 3962
[78] Zhang R and Willis R F 2001 *Phys. Rev. Lett.* **86** 2665
[79] Mukherjee T, Sahoo S, Skomski R, Sellmyer D J and Binek C 2009 *Phys. Rev. B* **79** 144406
[80] Thota S, Ghosh S, Nayak S, Joshi D C, Pramanik P, Roychowdhury K and Das S 2017 *J. Appl. Phys.* **122** 124304
[81] Xu X, Mellinger C, Cheng Z G, Chen X and Hong X 2022 *J. Appl. Phys.* **132** 020901
[82] Hara Y, Yoshino K, Tsujie A, Shimada T and Nagahama T 2023 *AIP Adv.* **13** 025162
[83] Shen Y, Kan D, Tan Z, Wakabayashi Y and Shimakawa Y 2020 *Phys. Rev. B* **101** 094412
[84] Kim J and Dho J 2023 *Thin Solid Films* **781** 139978
[85] Lv H, Huang X C, Zhang K H L, Bierwagen O and Ramsteiner M 2023 *Adv. Sci.* **10** 2302956
[86] Zheng B, Ji X, Xue M, Jia C, Kang C, Zhang W, Yang J, Tian M and Chen X 2024 *J. Phys.: Condens. Matter* **36** 275701
[87] Wang Y, Wu Y, Liu S, Xi Z, Hou P, Han Y and Wu D 2024 *Appl. Phys. Lett.* **124** 021904
[88] Dawn R, Pramanik B, Das K, Tjiu W W, Aabdin Z, Ghosh A, Sahoo S K, Amemiya K, Kandasami A and Singh V R 2024 *J. Appl. Phys.* **136** 143904
[89] Cullity B 1956 *Elements of X-ray Diffraction* (*Addison-Wesley Metallurgy Series*) (Addison-Wesley Publishing Company) (available at: https://books.google.co.jp/books?id=XJVCgGFTODMC)
[90] Attfield J P 1990 *Nature* **343** 46
[91] Xiao Y, Wittmer D E, Izumi F, Mini S, Graber T and Viccaro P J 2004 *Appl. Phys. Lett.* **85** 736
[92] Coey J M D 2010 *Magnetism and Magnetic Materials* (Cambridge University Press)
[93] Miyajima H, Sato K and Mizoguchi T 1976 *J. Appl. Phys.* **47** 4669
[94] Harrison W A 1980 *Electronic Structure and the Properties of Solids* (Dover Publications)
[95] Birss R R 1966 *Symmetry and Magnetism* vol 3 (Elsevier Science & Technology)
[96] Newnham R 2004 *Properties of Materials: Anisotropy, Symmetry, Structure* (OUP Oxford) (available at: https://books.google.co.jp/books?id=1eLPpuRpaNcC)
[97] Grimmer H 1993 *Acta Crystallogr. A* **49** 763
[98] Grimmer H 2017 *Acta Crystallogr. A* **73** 333
[99] Gallego S V, Etxebarria J, Elcoro L, Tasci E S and Perez-Mato J M 2019 *Acta Crystallogr. A* **75** 438
[100] Onsager L 1931 *Phys. Rev.* **37** 405
[101] Wills A S, Zhitomirsky M E, Canals B, Sanchez J P, Bonville P, de Réotier P D and Yaouanc A 2006 *J. Phys.: Condens. Matter* **18** L37
[102] Dzyaloshinsky I 1958 *J. Phys. Chem. Solids* **4** 241
[103] Moriya T 1960 *Phys. Rev.* **120** 91
[104] Onose Y, Ideue T, Katsura H, Shiomi Y, Nagaosa N and Tokura Y 2010 *Science* **329** 297
[105] Xiang H J, Kan E J, Whangbo M-H, Lee C, Wei S-H and Gong X G 2011 *Phys. Rev. B* **83** 174402
[106] Šmejkal L, González-Hernández R, Jungwirth T and Sinova J 2020 *Sci. Adv.* **6** eaaz8809
[107] Šmejkal L, Sinova J and Jungwirth T 2022 *Phys. Rev. X* **12** 040501
[108] Šmejkal L, Sinova J and Jungwirth T 2022 *Phys. Rev. X* **12** 031042
[109] Cheong S-W and Huang F-T 2024 *npj Quantum Mater.* **9** 13
[110] Leeb V, Mook A, Šmejkal L and Knolle J 2024 *Phys. Rev. Lett.* **132** 236701
[111] Yuan L-D, Wang Z, Luo J-W, Rashba E I and Zunger A 2020 *Phys. Rev. B* **102** 014422
[112] Mazin I (The PRX ed) 2022 *Phys. Rev. X* **12** 040002
[113] Bhowal S and Spaldin N A 2024 *Phys. Rev. X* **14** 011019
[114] Chen X, Ren J, Zhu Y, Yu Y, Zhang A, Liu P, Li J, Liu Y, Li C and Liu Q 2024 *Phys. Rev. X* **14** 031038
[115] Yan H, Zhou X, Qin P and Liu Z 2024 *Appl. Phys. Lett.* **124** 030503
[116] Xiao Z, Zhao J, Li Y, Shindou R and Song Z-D 2024 *Phys. Rev. X* **14** 031037
[117] Watanabe H, Shinohara K, Nomoto T, Togo A and Arita R 2024 *Phys. Rev. B* **109** 094438
[118] Naka M, Hayami S, Kusunose H, Yanagi Y, Motome Y and Seo H 2019 *Nat. Commun.* **10** 4305